

# **HHS Public Access**

Author manuscript

Concepts Magn Reson Part A Bridg Educ Res. Author manuscript; available in PMC 2016 May 01.

Published in final edited form as:

Concepts Magn Reson Part A Bridg Educ Res. 2015 May 1; 44(3): 138-149. doi:10.1002/cmr.a.21339.

# **Edge Sharpness Assessment by Parametric Modeling: Application to Magnetic Resonance Imaging**

R Ahmad<sup>1</sup>, Y Ding<sup>2</sup>, and OP Simonetti<sup>3,4</sup>

<sup>1</sup>Department of Electrical and Computer Engineering, The Ohio State University, Columbus, OH, USA

<sup>2</sup>United Imaging, Houston, TX, USA

<sup>3</sup>Department of Internal Medicine, Division of Cardiovascular Medicine, The Ohio State University, Columbus, OH, USA

<sup>4</sup>Department of Radiology, The Ohio State University, Columbus OH, USA

#### **Abstract**

In biomedical imaging, edge sharpness is an important yet often overlooked image quality metric. In this work, a semi-automatic method to quantify edge sharpness in the presence of significant noise is presented with application to magnetic resonance imaging (MRI). The method is based on parametric modeling of image edges. First, an edge map is automatically generated and one or more edges-of-interest (EOI) are manually selected using graphical user interface. Multiple exclusion criteria are then enforced to eliminate edge pixels that are potentially not suitable for sharpness assessment. Second, at each pixel of the EOI, an image intensity profile is read along a small line segment that runs locally normal to the EOI. Third, the profiles corresponding to all EOI pixels are individually fitted with a sigmoid function characterized by four parameters, including one that represents edge sharpness. Last, the distribution of the sharpness parameter is used to quantify edge sharpness. For validation, the method is applied to simulated data as well as MRI data from both phantom imaging and cine imaging experiments. This method allows for fast, quantitative evaluation of edge sharpness even in images with poor signal-to-noise ratio. Although the utility of this method is demonstrated for MRI, it can be adapted for other medical imaging applications.

#### **Keywords**

edge; boundary; sharpness; modeling; sigmoid; MRI

#### INTRODUCTION

The quality of biomedical images can be characterized by a number of different measures such as signal-to-noise ratio (SNR), contrast-to-noise ratio (CNR), artifacts, and edge

<sup>\*</sup>Corresponding author. Rizwan Ahmad\*, 460 W 12<sup>th</sup> Ave, BRT 326, Columbus, OH 43210, USA, Phone: 1-614- 247-8717, Fax: 1-614-247-8277, ahmad.46@osu.edu, Orlando P. Simonetti, 460 W 12<sup>th</sup> Ave, BRT 316, Columbus, OH 43210, USA, Phone: 1-614-293-0739, Orlando.Simonetti@osumc.edu.

sharpness. Although there exist standard techniques to quantify SNR and CNR (1–4), image sharpness has not been studied extensively, especially in the realm of magnetic resonance imaging (MRI). In this work, we describe a semi-automatic tool to assess image sharpness and demonstrate its application to MRI.

Advances in MRI continue to improve its accuracy and precision in the detection and characterization of disease and injury. These advances, in turn, have spawned a plethora of pMRI data acquisition and image reconstruction methods (5–7), which differ from one another in terms of computation speed, SNR, level of artifacts, fidelity to the ground truth, and image sharpness. Iterative reconstruction methods based on regularized least-squares, in particular, have attracted attention recently (8,9). These methods invariably offer a trade-off between SNR and image sharpness. This trade-off is controlled by the extent of regularization, which is often selected using ad hoc criteria.

Edges in biomedical images often carry physiologically important information and play a central role in image quantification. For example, in cardiac MRI, images are often analyzed to quantify physiologically relevant parameters such as ejection fraction (10), myocardial wall motion (11), blood flow velocity (12), and myocardial perfusion (13). The estimation of these parameters is often performed using image segmentation, which invariably involves locating edges of various anatomic features. Several methods have been proposed to assess image sharpness, but many of these may not be suitable for MRI. For example, nonparametric sharpness measures that rely on computing local gradient values of the image intensity (14,15) or kurtosis in a transformed domain (16) are not suitable for low SNR conditions (a common occurrence in MRI, especially with the use of pMRI) because both gradient and kurtosis values are sensitive to noise. Likewise, the commonly used sharpness assessment method based on measuring the 10-90% rise distance (17) in the image domain or the full width at half maximum (FWHM) distance in the derivative domain of image (18) are also susceptible to image noise because such methods do not fully utilize the entire available data to measure sharpness. The techniques based on parametric modeling of edges, which are more robust to noise, have been used to quantify sharpness for optical images (19,20) and to study margin sharpness of lesions in CT (21). We propose a method, called Edge Sharpness Assessment by Parametric modeling (ESAP), based on sigmoidal modeling of edges, that attempts to provide a sharpness measure that is robust under low SNR conditions. More importantly, the ESAP method is equipped to handle the complexities of MRI images such as low SNR, tissue-specific boundary sharpness, and anisotropic blurring.

#### MATERIALS AND METHODS

In this section, we describe the proposed technique used for ESAP. The materials and methods used for conducting simulations and MRI experiments and also discussed in this section.

#### **2.1 ESAP**

The entire method can be broken down into four steps: edge selection, intensity profile extraction, curve fitting, and hypothesis testing. Each of these four steps is described below.

**2.1.1 Step-1 – Edge selection**—e used the Canny edge detector (CED) to extract a binary edge map from an  $M \times N$  grayscale image, I(x, y) (22). CED finds edges by looking for local maxima of the gradient of I(x, y). Typically, implementation of CED requires choosing values for two thresholds (high and low) and a standard deviation of the Gaussian filter. We employed the in-built Matlab (Mathworks, MA) function with high-threshold = 0.1, low-threshold = 0.04 and standard deviation of the Gaussian filter = 1.5. In addition to the binary edge map, g(x, y), gradient orientation,  $\theta(x, y)$ , was also obtained at each edge pixel by

$$\theta(x,y) = \arctan\left(\frac{\nabla_y(G*I(x,y))}{\nabla_x(G*I(x,y))}\right) \quad \text{(1)}$$

where  $\nabla_x$  and  $\nabla_y$  compute image gradients in x (horizontal) and y (vertical) directions, respectively, G represents the 2D Gaussian filter used in CED, and '\*' represents 2D convolution.

The edge maps generated using CED invariably contain branches. The image intensity at or around the bifurcation of two or more edges may not comply with the expected shape of an edge. Therefore, the pixels at or around edge bifurcation points should be discarded from further consideration. Here, we have used template matching to locate and remove bifurcations. Since CED generates edge contours that are one pixel wide, a total of sixteen  $3 \times 3$  binary templates (Figure 1) are adequate to represent all possible bifurcation configurations. To locate bifurcations via template matching, the binary edge map, g(x, y), is convolved with each of the sixteen templates. Since each template has exactly four non-zero entries, the result of the convolution, at each pixel, can only reach four if the same non-zero entries are also present in the  $3 \times 3$  window around that pixel. Therefore, the instances (locations in the image), where the result of the 2D convolution is equal to four, indicate presences of bifurcations. The resulting bifurcation-free map is denoted by  $g_b(x, y)$ .

An image in MRI may contain edges with variable inherent sharpness; for example, if the boundary between two tissues is not orthogonal to the image slice, partial volume effects may blur the boundary. Also, the choice of image reconstruction and filtering methods may impact different edges differently. For example, temporal filtering or regularization may blur dynamic edges more than stationary edges (23,24). Therefore, any global measure for edge sharpness may not be meaningful, as it may not reflect the sharpness of diagnostically important features. As a result, instead of analyzing all of the edges present in  $g_b(x, y)$ , we let the user select one or more edges-of-interest (EOI). An edge, which is defined as a continuous (8-connectivilty) contour in  $g_b(x, y)$ , was selected by clicking the computer mouse after bringing the cursor over any of the edge pixel. The resulting map with user selected edge or edges is denoted by  $g_u(x, y)$ .

Not every pixel in  $g_u(x, y)$  is a reasonable candidate for sharpness assessment. For example, it has been previously shown that interaction between two nearby edges may result in edge shape distortion (19). To counter the effects of nearby edges, the following constraint can be enforced in the selection of edge pixels: discard all pixels in  $g_u(x, y)$  if they have another non-zero pixel within a distance d in the gradient direction  $\theta(x, y)$ . Although it is possible to

identify pixels that do not comply with the above mentioned constraint by searching in the direction of local gradient for each non-zero pixel in  $g_u(x, y)$ , we have instead adopted an alternative approach that is approximate but extremely simple and fast. Here, the pixels,  $\mathcal{M}(x, y)$ , that do not comply with the constraint are identified by using a sequence of four morphological filters, generating

$$\mathcal{M}(x,y) = \mathcal{D}(\mathcal{D}^c(\mathcal{D}^c(\mathcal{D}(g(x,y),S_d),S_d),S_d),S_2), \quad (2)$$

where  $\mathscr{D}$  and  $\mathscr{D}^c$  represent dilation and erosion operators, respectively, and  $S_d$  and  $S_2$  represent disk-shaped structuring elements with diameters of d and 2 pixels, respectively. In this sequence of morphological filters, the first filter (the inner most  $\mathscr{D}$  in Equation 5) dilates the edges and in the process fuses the neighboring edges if they are less than or equal to d pixels apart, the second erosion filter removes the effect of dilation except for the areas where application of the first filter resulted in edge fusion, the third erosion filter removes original edges in g(x, y), leaving behind only the pixels which are less than d pixels away from two edges but are not part of g(x, y), and the last filter reinstates the non-zero pixels in g(x, y) that are connected to the pixels identified in the previous step. The pixels identified by  $\mathscr{M}(x, y)$  are eliminated by setting all pixels in g(x, y) that have corresponding non-zero values in  $\mathscr{M}(x, y)$  to zero, yielding,

$$g_m(x,y)=g_u(x,y)\circ \mathscr{M}^c(x,y),$$
 (3)

where  $\circ$  represents a point-by-point logical AND operator, and  $\mathcal{M}$  is the pixel-wise binary inverse of  $\mathcal{M}$ .

Depending on the data acquisition and image reconstruction methods, an MRI image may exhibit anisotropic sharpness (14). For example, to accelerate acquisition, it is not uncommon to reduce the number of phase encoding (PE) steps while maintaining the number of samples along the readout direction. This reduction, however, results in a sharpness penalty in the PE direction. Therefore, a sharpness assessment method for MRI should provide the option of direction-dependent assessment of image sharpness. In this work, we let the user define an admissible range of gradient directions,  $\theta$ , for ESAP. This way, a pixel in  $g_m(x, y)$  is only considered for further analysis if the corresponding  $\theta(x, y)$  value belongs to a predefined range,  $\theta$ . Let  $g_f(x, y)$  denote a set of all such pixels. Figure 2 provides a pictorial representation of the various procedures involved in Step-1. Only non-zero pixels in  $g_f(x, y)$  are used for further analysis of sharpness assessment.

**2.1.2 Step-2 – Profile extraction**—or each non-zero pixel in  $g_f(x, y)$ , we read the corresponding intensity profile from I(x, y). Although spatial filtering was employed as a part of CED, the intensity profiles are read directly from unfiltered I(x, y). Therefore, the sharpness reported in ESAP is not biased by the smoothing filter used in CED. Each intensity profile read from I(x, y) is sampled along a small line segment that is locally perpendicular to the edge contour or, equivalently, in the direction of  $\theta(x, y)$ . A 1D intensity profile for the pixel (x, y) can be written as

$$p(\rho, x, y, \theta) = I(x + \rho \cos(\theta(x, y)), y + \rho \sin(\theta(x, y))),$$
 (4)

where  $p(\rho, x, y, \theta)$  is the intensity profile centered at location (x, y), and  $\rho$  is a vector that uniformly discretizes the interval (-L/2, L/2), with the positive number L determining the spatial extent, in terms of pixels, of the intensity profile. Limiting L - 2d + 1 ensures that the profiles carry information about the intended edge alone and are not contaminated by neighboring edges.

For an arbitrary  $\theta$  value, the samples along  $\rho$  may not fall on a Cartesian grid. Therefore, an interpolation is required to construct 1D intensity profiles from a 2D image. Here, we used natural neighbor interpolation (25) with oversampling by a factor of r, which means each intensity profile contains  $r \times L$  samples. For brevity, we will represent an intensity profile by  $p(\rho)$ . An illustration of the process to read an intensity profile is depicted in Figure 3.

**2.1.3 Step-3**– **Least-squares curve fit**—Each profile is individually fitted with a sigmoid function, *f*, given by

$$f(\rho; a_0, a_1, a_2, s) = \frac{a_1}{1 + 10^{s(a_0 - \rho)}} + a_2,$$
 (5)

where  $a_0$  determines the center location  $a_1$ , determines the vertical range  $a_2$ , defines the vertical offset, and s quantifies the growth rate or sharpness of the sigmoid. For brevity, we will denote the sigmoid function in Equation 5 by  $f(\rho)$ .

For a measured intensity profile  $p(\rho)$ , the parameter s, along with other nuisance parameters, can be estimated by fitting  $p(\rho)$  with  $f(\rho)$ , giving

$$(\tilde{a}_0, \tilde{a}_1, \tilde{a}_2, \tilde{s}) = \underset{a_0, a_1, a_2, s}{\operatorname{argmin}} \| \boldsymbol{p} - \boldsymbol{f} \|_2^2,$$
 (6)

where p and f represent vector forms of  $p(\rho)$  and  $f(\rho)$ , respectively. The sigmoid function for four different values s of is shown in Figure 4a, and the least-squares curve-fitting of the profile in Figure 3b is shown in Figure 4b.

**2.1.4 Step-4 – Hypothesis testing**—Since there are multiple intensity profiles (one for each non-zero pixel in  $g_f(x, y)$ ), the sharpness of each image is represented by a distribution of s. Therefore, comparing the sharpness of multiple images can be posed as a hypothesis testing problem. In this work, a multiple comparison test (MCT) was performed to compare sharpness across different images. First, balanced one-way ANOVA was employed to evaluate the hypothesis that all images in a dataset have the same mean sharpness against the alternative that the mean sharpness is not the same across all images. To further identify which pairs of images are significantly different in terms of mean sharpness, Tukey's honestly significant difference criterion (also called Tukey–Kramer method) was employed with  $\alpha = 0.05$ .

### 2.2 Study Protocol and Experimental Validation

The simulation studies were conducted to highlight the noise robustness of ESAP compared to two previous sharpness quantification methods. For experimental validation, the proposed method was applied to data from phantom imaging as well as in vivo imaging. For phantom

imaging, the ESAP method was employed to evaluate direction dependent loss in edge sharpness due to reduction in the number of PE steps. For in vivo imaging, the ESAP method was used to quantify loss in edge sharpness due to smoothing effects of regularization. The instrument settings and the values of the algorithmic parameters used in these studies are described below.

**2.2.1 Simulation**—A 256 × 256 digital image was simulated in Matlab. The pixels in the left-half of the image were set to zero, while the pixels in the right-half of the image were set to one, creating a perfect vertical edge in the middle. To artificially vary edge sharpness, the image was convolved with a 2D Gaussian filter, with the standard deviation of  $\sigma_b$  pixels. The value of  $\sigma_b$  was varied from 0.4 pixels to 1.8 pixels in the increments of 0.2 pixels. Each of the resulting eight images was contaminated with eight different levels of additive white Gaussian noise with standard deviation of  $\sigma_n$ . The value of  $\sigma_n$  was varied from  $4 \times 10^{-3}$  to  $256 \times 10^{-3}$  with the geometric ratio of 2. There were a total of 64 different images, each with a different combination of  $\sigma_b$  and  $\sigma_n$ . Four such images are shown in Figure 5.

For comparison, we implemented two other methods that have been previously reported for edge sharpness quantification. The first method is based on the rise-rate of the image intensity along the lines perpendicular to the edge; rise-rate is defined to be the reciprocal of the 10–90% rise distance (17). This method is termed as edge sharpness assessment by riserate (ESARR). The second method is based on the reciprocal of FWHM of the denoised, first-derivative map of the image along the lines perpendicular to the edge. This method, called edge sharpness assessment by denoised-derivative (ESADD), has been applied to MR angiography (MRA) to evaluate the sharpness of blood vessels (18,26). Our implementation of ESADD, however, differs from the implementation used in MRA in two aspects. First, we employed a non-recursive, finite-impulse-response (FIR) approximation to Gaussian filter (with standard deviation of 1 pixel) instead of using an infinite-impulse-response Deriche filter (27) that employs computationally efficient recursive processing to denoise images prior to computing the first-derivative map. Using contemporary computing resources, the additional computation cost associated with non-recursive FIR filtering is no longer a concern. Second, since we are dealing with a single edge as opposed to two closelyspaced parallel edges of blood vessels, we used the reciprocal of FWHM (compared to the reciprocal of the separation between two maxima) as a measure of sharpness.

Applying a denoising filter is an integral part of the ESADD method, but this denoising step changes the inherent image sharpness. Therefore, the results from ESADD cannot be directly compared with ESAP and ESARR methods, which do not require denoising. To ensure a fair comparison in the simulation studies, however, ESAP and ESARR were also applied on the denoised images used in ESADD.

To evaluate the impact of noise on sharpness measurement, the estimated sharpness was compared (using MCT) for images with  $\sigma_b$  fixed and varying level of  $\sigma_n$  and also for images with fixed  $\sigma_n$  and varying levels of  $\sigma_b$ . The analysis was performed for each of the three sharpness quantification method, i.e., ESAP, ESARR, and ESADD. For the ESAP implementation, we selected, r = 8, d = 3, and L = 2d + 1. To ensure that the sharpness was measured form the same exact region  $g_f(x, y)$ , constructed from the image with highest SNR

(when  $\sigma_n$  is varied for a fixed  $\sigma_b$ ) or the highest sharpness (when  $\sigma_b$  is varied for a fixed  $\sigma_n$ ) was used for all the images included in the comparison.

**2.2.2 Phantom imaging**—A circular cross-section of a water bottle was imaged on a 1.5 T MRI system (MAGNETOM Avanto, Siemens Medical Solutions, Malvern, PA) using a 12-channel head coil array. The imaging parameters were: 120 × 120 matrix size, GRE sequence, 5 mm slice thickness, 250 × 250 mm<sup>2</sup> field-of-view (FOV), and no downsampling was employed along the PE direction. The individual coil reconstructions (data not shown) were obtained by 2D inverse Fourier transform of the k-space data. The final reconstruction was obtained by SoS combination of the individual coil reconstructions. A total of eight datasets were collected with the same imaging parameters except for the number of PE steps. Starting from 100% (120) PE steps for the first dataset, the subsequent datasets had 90%, 80%, 70%, 60%, 50%, 40%, and 30% PE steps, respectively, as shown in Figure 6.

To analyze the anisotropic impact of reducing PE on edge sharpness, two sections of the circular edge were separately processed. First, the sharpness for the edge sections nearly orthogonal to the PE direction was measured. Then, the sharpness for the edge sections nearly parallel to the PE direction was measured. The two sections were selected by adjusting admissible range of  $\theta$ . For the ESAP implementation, we selected, r = 8, d = 3, and L = 2d + 1. To ensure that the sharpness was measured form the same exact region  $g_f(x, y)$ , constructed from the image with 100% PE steps was used for all other images.

**2.2.3 Cine imaging**—Fully sampled segmented cine data were collected from a healthy volunteer on a 1.5 T clinical Siemens scanner using a 32-channel body array coil. Acquisition parameters: FOV  $293 \times 360 \text{ mm}^2$ , matrix size  $156 \times 192$ , SSFP pulse sequence, 31 ms temporal resolution, 8 mm slice thickness, TE 1 ms, TR 2.6 ms, receiver bandwidth 1371 Hz/pixel, 12 lines/segment, flip angle 75°, and 14 total frames. The data were retrospectively downsampled (R = 5) and reconstructed with regularized SPIRiT (7) for three different regularization strengths,  $\lambda$ . A representative frame is shown in Figure 7. The edge sharpness was measured for manually selected myocardial boundary. For the ESAP implementation, we selected, r = 8, d = 3, and L = 2d + 1. To ensure that the sharpness was measured form the same exact region,  $g_f(x, y)$  constructed from the fully sampled reference was used for all other images.

## **RESULTS**

The simulation, phantom imaging, and MRI cine results are reported in this section. The horizontal bars in Figures 8, 9f and 10d represent the comparison intervals from MCT. The intervals that are disjoint represent a significant difference, while the overlapping intervals represent a lack of significant difference.

#### 3.1 Simulation

The simulation results are reported in Figure 8. Figure 8a compares the estimated sharpness for a fixed value of  $\sigma_b$  (true blurring) and eight different values of  $\sigma_n$  (SNR). For each of the methods, the mean sharpness for the highest SNR image ( $\sigma_n = 4 \times 10^{-3}$ ) was normalized to one. The overlapping comparison intervals indicate that the change in SNR did not result in

a significant change in measured sharpness for ESAP, which was not the case for ESARR and ESADD. Figure 8b reports the measured sharpness for eight different input values of  $\sigma_b$  for moderate (first row of Figure 8b) and low (second row of Figure 8b) SNR values, highlighting the ability of the three methods to capture small change in sharpness in the presence of noise.

#### 3.2 Phantom imaging

The reconstructed images, for eight different numbers of PE steps, are shown in Figure 6. The ESAP sharpness results are reported in Figure 9. Figure 9a presents the image with 100% PE and Figure 9b represents edge map obtained by applying CED on the image in Figure 9a. Figure 9c shows the user selected EOI. Figures 9d and 9e represent horizontal and vertical sections of the edge selected by controlling  $\theta$ . Figure 9f represents ESAP results for both horizontal and vertical sections of the edges. As revealed by the comparison intervals in Figure 9f, the sharpness of the horizontal edges (Figure 9d) does not change significantly even with large changes in the number of PE steps, while the sharpness of vertical edges (Figure 9e) changes significantly with every 10% change in the number of PE steps.

# 3.3 Cine imaging

The reconstructed images for four different regularization strengths,  $\lambda$ , are shown in Figure 7. For better visualization, only a 54 × 74 ROI is shown. The edge sharpness results, for the manually selected myocardial boundary, are reported in Figure 10. Figure 10a shows a fully sampled reference image. Figures 10b and 10c show the output of CED and user selected EOI, respectively. Figure 10d shows the results of MCT for four different images shown in Figure 7.

### **4 DISCUSSION**

While there exist established methods for SNR and CNR measurements, quantification of image sharpness has not been studied extensively, especially for MRI applications. Here, we have proposed and experimentally validated a sharpness measurement method for MRI. In contrast to the previously reported methods, the proposed method is designed to accommodate the complexities of real MRI data. First, ESAP allows sharpness quantification from one or more EOI selected by the user. This local approach is suitable for MRI because images in MRI do not exhibit uniform sharpness due to either the inherently heterogeneous content of the image or data processing methods that may induce contentdependent blurring. For example, Karhunen-Loeve transform based de-noising of cardiac MRI tends to blur dynamic edges more than static edges (24). Second, we have used an array of exclusion criteria to remove edges or parts of edges that are expected to be poor candidates for sharpness assessment. For example, we have identified and removed bifurcation points as well as edges that reside in the vicinity of other edges. Third, the method allows for separating edge pixels based on their spatial orientation. Therefore, ESAP is valuable when studying images with direction-dependent variations in spatial resolution. Fourth, the proposed method is suitable for low SNR conditions because it does not suffer from the noise-induced bias that affects gradient-based methods. Last, ESAP generates a

histogram of *s* and thus enables hypothesis testing for more robust comparison of two images. The proposed method was implemented in Matlab. The total computation time, for the images considered, was in the range of 2 to 4 s per image, using ordinary, contemporary computing resources.

Compared to ESARR and ESADD, ESAP offers a distinct advantage: robustness against noise, including lack of noise-induced bias. For additive Gaussian noise, s computed by ESAP is an unbiased estimate of true sharpness, s. In contrast, ESARR and ESADD are prone of noise-induced bias in sharpness quantification. The simulation results in Figure 8 illustrate that both ESARR and ESADD suffer from noise induced bias, especially for low SNR datasets. For ESARR, the sharpness of images with  $\sigma_n=32\times10^{-3}$  was significantly underestimated compared to the highest SNR image. For ESADD, only the image with  $\sigma_n=512\times10^{-3}$  had a significantly different sharpness compared to the highest SNR image. In addition, unlike ESARR and ESADD, ESAP utilizes all the data samples along the profile, making it more robust to noise. As illustrated in Figure 8b, for moderate SNR, all three methods are effective in distinguishing small differences in the true edge sharpness. At low SNR, however, the ability of ESAP to discern small sharpness differences is superior to other two methods, especially ESADD. Collectively, the results presented in Figure 8 illustrate that ESAP is capable of operating in the presence of significant noise and can compare images with different noise levels.

For experimental validation, ESAP is applied to quantify the impact of reducing the number of PE steps, as demonstrated in Figures 6 and 9. Since the PE is in the horizontal direction (left to right), the reduction does not impact all edge pixels equally. We anticipate, the near-vertical sections of the circular edge are affected the most, while the near-horizontal sections are affected the least. This direction-dependent variation in image sharpness – not readily evident from the visual inspection of Figure 6 – is effectively captured by the proposed method, with each 10% reduction in PE resulting in significant sharpness loss for near-vertical sections of the circular edge.

The proposed method was used to study the impact of regularization on edge sharpness – an aspect often neglected in the MRI literature. For in vivo data, we found that signal-to-noise monotonically improved with increase in  $\lambda$ . Hence, without considering the edge sharpness, one may conclude that reconstructions with the strongest regularization (i.e.,  $\lambda = 100 \times 10^{-2}$ ), shown in Figure 7d, are superior. However, the ESAP-based measurements clearly indicate that image in Figure 5d have inferior sharpness compared to the images with lower regularization values, providing a more comprehensive evaluation of image quality and a clearer understanding of the trade-offs involved in selecting image reconstruction parameters.

The proposed method is semi-automatic; in addition to selecting EOI and choosing parameters for CED, the user is also responsible for assigning values to these tuning parameters: d, L, and r. The edge map provided by CED is merely used to select EOI; therefore, a precise selection of CED parameters is not crucial for ESAP. In this work, we used an in-built Matlab function with its default settings to implement CED. The value of r controls oversampling along the intensity profiles. For the data presented here, there was

practically no difference in the results for a wide range of oversampling factors. An optimal choice for d requires knowledge of the underlying blurring function. A wider blurring function can convolute edges across a larger distance and would require a larger value of d; however, using large values excludes more edge pixels from consideration. If the extent of the blurring function is not known, a conservatively large value for d can be used as long as this value is not too large to exclude a significant fraction of pixels on EOI. For most applications, we expect 2 - d - 5 to be adequate. If L is selected too small, the resulting profile does not cover the entire edge. On the other hand, if L is selected too large, the resulting profile extends far beyond the edge and may encompass other unwanted features. Limiting L - 2d + 1 ensures that the profiles carry information about the intended edge alone and are not contaminated by neighboring edges.

The objective of this work is to develop a quantitative method that can objectively access changes in the edge sharpness that may result from the use of different acquisition, reconstruction, and processing methods. However, the sharpness measure provided by the ESAP method may or may not match the visual perception of image sharpness (28). Also, caution should be observed in applying this approach to either measure absolute sharpness of an image or to compare images with different content. For such cases, a comparison based on the proposed approach may not differentiate the blurring introduced due to data processing methods from the inherent sharpness differences of the images or anatomical features. Therefore, a comparison among identical images that only differ in sharpness, SNR, and CNR is a more appropriate application of this method.

#### **5 CONCLUSIONS**

We have presented a semi-automatic edge sharpness assessment method suitable for MRI applications. The user, via graphical user interface, selects one or more edges from the image edge map. Several exclusion criteria are then applied to eliminate sections of the edges that might not be appropriate for sharpness assessment. Across each remaining edge pixel, the image intensity profiles are read and fitted with a sigmoid function. The distribution of the sharpness parameter of the sigmoid function quantifies image sharpness. We have applied the method to simulated as well as experimental data, including in vivo MRI cine images. The results indicate that this is a viable method to quantify changes in image sharpness that might not be readily identified by naked eye.

# **Acknowledgment**

The project described was partially supported by Award Number R01HL102450 from the National Heart, Lung, And Blood Institute.

# **REFERENCES**

- 1. Ding Y, Chung YC, Jekic M, Simonetti OP. A new approach to autocalibrated dynamic parallel imaging based on the Karhunen-Loeve transform: KL-TSENSE and KL-TGRAPPA. Magn. Reson. Med. 2011; 65:1786–1792. [PubMed: 21254210]
- 2. Reeder SB, Wintersperger BJ, Dietrich O, Lanz T, Greiser A, Reiser MF, Glazer GM, Schoenberg SO. Practical approaches to the evaluation of signal-to-noise ratio performance with parallel

- imaging: Application with cardiac imaging and a 32-channel cardiac coil. Magn. Reson. Med. 2005; 54:748–754. [PubMed: 16088885]
- Heverhagen JT. Noise Measurement and Estimation in MR Imaging Experiments. Radiology. 2007; 245:638–639. [PubMed: 18024445]
- Wada Y, Hara T, Miyati T. Basic assessment of the CNR measurement method of MRI system in phantom-suggestion for improvement in the CNR evaluation method. Nihon Hoshasen Gijutsu Gakkai Zasshi. 2008; 64:268–276. [PubMed: 18311033]
- Pruessmann KP. Encoding and reconstruction in parallel MRI. Magn. Reson. Med. 2006; 19:288– 299.
- Zhang J, Liu C, Moseley ME. Parallel reconstruction using null operations. Magn. Reson. Med. 2011; 66:1241–1253. [PubMed: 21604290]
- 7. Lustig M, Pauly JM. SPIRiT: Iterative self-consistent parallel imaging reconstruction from arbitrary k-space. Magn. Reson. Med. 2010; 64:457–471. [PubMed: 20665790]
- Lustig M, Donoho D, Pauly JM. Sparse MRI: The application of compressed sensing for rapid MR imaging. Magn. Reson. Med. 2007; 58:1182–1195. [PubMed: 17969013]
- 9. Ma, S.; Yin, W.; Zhang, Y.; Chakraborty, A. An efficient algorithm for compressed MR imaging using total variation and wavelets; IEEE Conf Comput Vis. Pattern Recognit; 2008. p. 1-8.
- Rossum AC, Van, Visser FC, Sprenger M, Eenige MJ, Van, Valk J, Roos JP. Evaluation of magnetic resonance imaging for determination of left ventricular ejection fraction and comparison with angiography. Am. J. Cardiol. 1988; 62:628–633. [PubMed: 3414556]
- 11. McVeigh ER. MRI of myocardial function: motion tracking techniques. Magn. Reson. Imaging. 1996; 4:137–150. [PubMed: 8847969]
- Evans AJ, Iwai F, Grist TA, Sostman HD, Hedlund LW, Spritzer CE, Negro-Vilar R, Beam CA, Pelc NJ. Magnetic resonance imaging of blood flow with a phase subtraction technique. In vitro and in vivo validation. Invest. Radiol. 1993; 28:109–115. [PubMed: 8444566]
- 13. Wilke NM, Jerosch-Herold M, Zenovich A, Stillman AE. Magnetic resonance first-pass myocardial perfusion imaging: Clinical validation and future applications. J. Magn. Reson. Imaging. 1999; 10:676–685. [PubMed: 10548775]
- Biasiolli L, Lindsay AC, Choudhury RP, Robson MD. Loss of fine structure and edge sharpness in fast-spin-echo carotid wall imaging: measurements and comparison with multiple-spin-echo in normal and atherosclerotic subjects. J. Magn. Reson. Imaging. 2011; 33:1136–1143. [PubMed: 21509872]
- 15. Chung Y-C, Wang J-M, Bailey RR, Chen S-W, Chang S-L. A non-parametric blur measure based on edge analysis for image processing applications. IEEE Conf Cyber Intel Sys. 2004; 1:356–360.
- Caviedes J, Gurbuz S. No-reference sharpness metric based on local edge kurtosis. IEEE Intl Conf Image Process. 2002; 3:53–56.
- 17. Fauver M, Seibel E, Rahn JR, Meyer M, Patten F, Neumann T, Nelson A. Three-dimensional imaging of single isolated cell nuclei using optical projection tomography. Opt. Express. 2005; 13:4210–4223. [PubMed: 19495335]
- 18. Etienne A, Botnar RM, Van Muiswinkel AMC, Boesiger P, Manning WJ, Stuber M. "Soap-Bubble" visualization and quantitative analysis of 3D coronary magnetic resonance angiograms. Magn. Reson. Med. 2002; 48:658–666. [PubMed: 12353283]
- 19. Wu, S.; Xie, S. An efficient blind method for image quality measurement; 7th Intl Conf Inform, Commun Signal Process; 2009. p. 1-5.
- 20. Dijk, J.; van Ginkel, M.; van Asselt, RJ.; van Vliet, LJ.; Verbeek, PW. A new sharpness measure based on Gaussian lines and edges; 8th Conf Adv Sch. Comput Imaging; 2001. p. 39-43.
- Xu J, Napel S, Greenspan H, Beaulieu CF, Agrawal N, Rubin D. Quantifying the margin sharpness of lesions on radiological images for content-based image retrieval. Med. Phys. 2012; 39:5405– 5418. [PubMed: 22957608]
- Canny J. A Computational Approach to Edge Detection. IEEE Trans. Pattern Anal. Mach. Intell. PAMI-8. 1986:679–698.
- 23. Blaimer M, Ponce IP, Breuer FA, Jakob PM, Griswold MA, Kellman P. Temporal filtering effects in dynamic parallel MRI. Magn. Reson. Med. 2011; 66:192–198. [PubMed: 21695723]

24. Ding Y, Chung Y-C, Raman SV, Simonetti OP. Application of the Karhunen-Loeve transform temporal image filter to reduce noise in real-time cardiac cine MRI. Phys. Med. Biol. 2009; 54:3909–3922. [PubMed: 19491455]

- 25. Sibson, R. A brief description of natural neighbor interpolation. In: Barnett, V., editor. Interpreting Multivariate Data. Chichester: John Wiley; 1981. p. 21-36.
- 26. Botnar RM, Stuber M, Danias PG, Kissinger KV, Manning WJ. Improved coronary artery definition with T2-weighted, free-breathing, three-dimensional coronary MRA. Circulation. 1999; 99:3139–3148. [PubMed: 10377077]
- 27. Deriche R. Fast algorithms for low-level vision. IEEE Trans PAMI. 1990; 12:78–87.
- 28. Ferzli, R.; Karam, L. Human Visual System Based No-Reference Objective Image Sharpness Metric; IEEE Int. Conf. Image Process; 2006. p. 2949-2952.

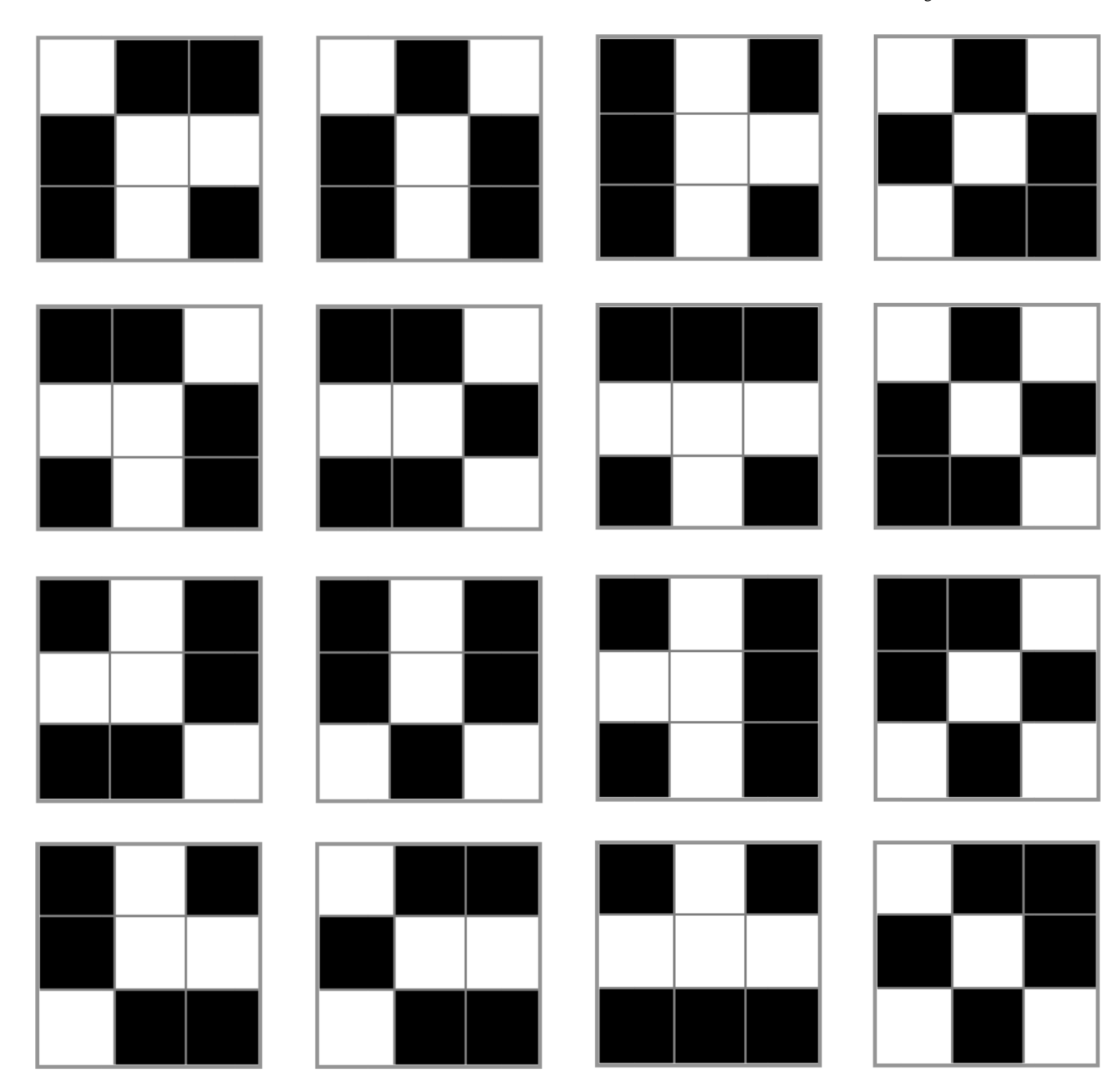


Figure 1. Sixteen  $3 \times 3$  templates used to detect bifurcations. Second, third, and fourth rows are obtained by 90°, 180°, and 270° rotations of row 1, respectively.

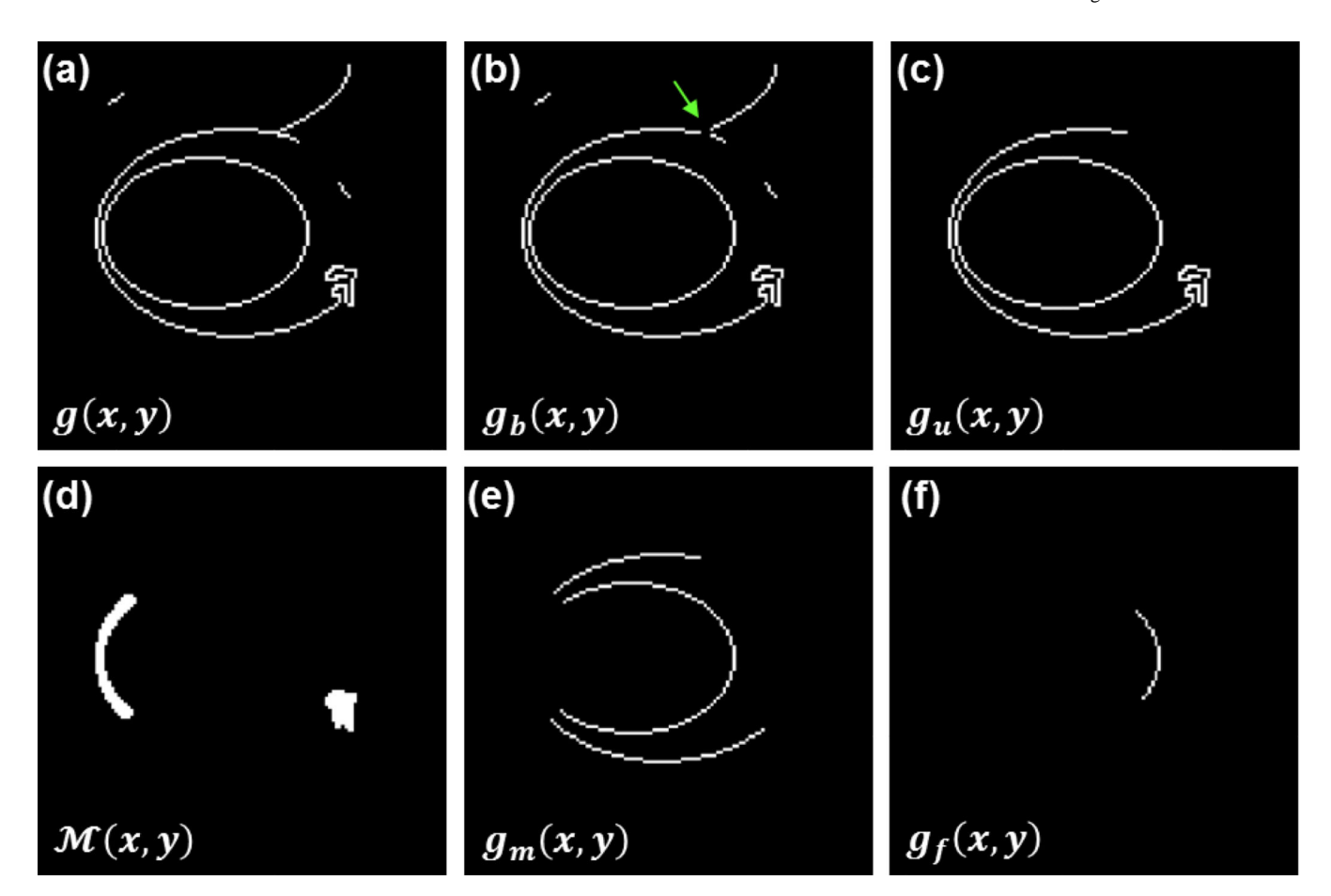


Figure 2. A visual illustration of the various procedures involved in Step-1 of ESAP. (a) A 128×128 digitally fabricated edge map that belongs to a hypothetical image (not shown). (b) The edge map in (a) with bifurcations removed. The pixel at the bifurcation (arrow) was located using template matching. (c) The edge map from (b) with two user selected edges,  $g_u(x, y)$ . (d) A binary map  $\mathcal{M}(x, y)$  generated by applying Equation 2 with d = 5. (e) Application of Equation 3 to subtract  $\mathcal{M}(x, y)$  from the edge map in (c) to generate  $g_m(x, y)$ . (f) Selection of pixels from (e) based on an arbitrary, user defined  $\theta = (-30^\circ, 30^\circ) \cup (150^\circ, 210^\circ)$ . This map corresponds to  $g_f(x, y)$ .

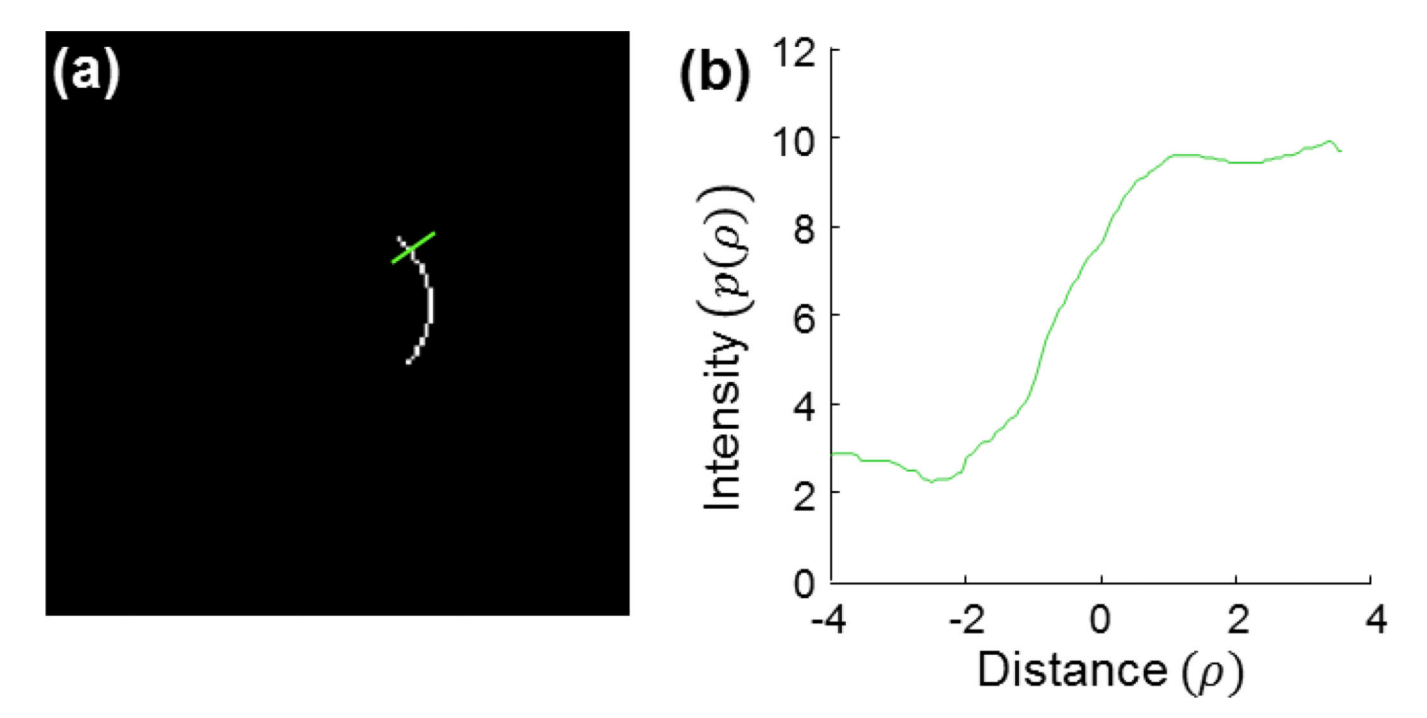
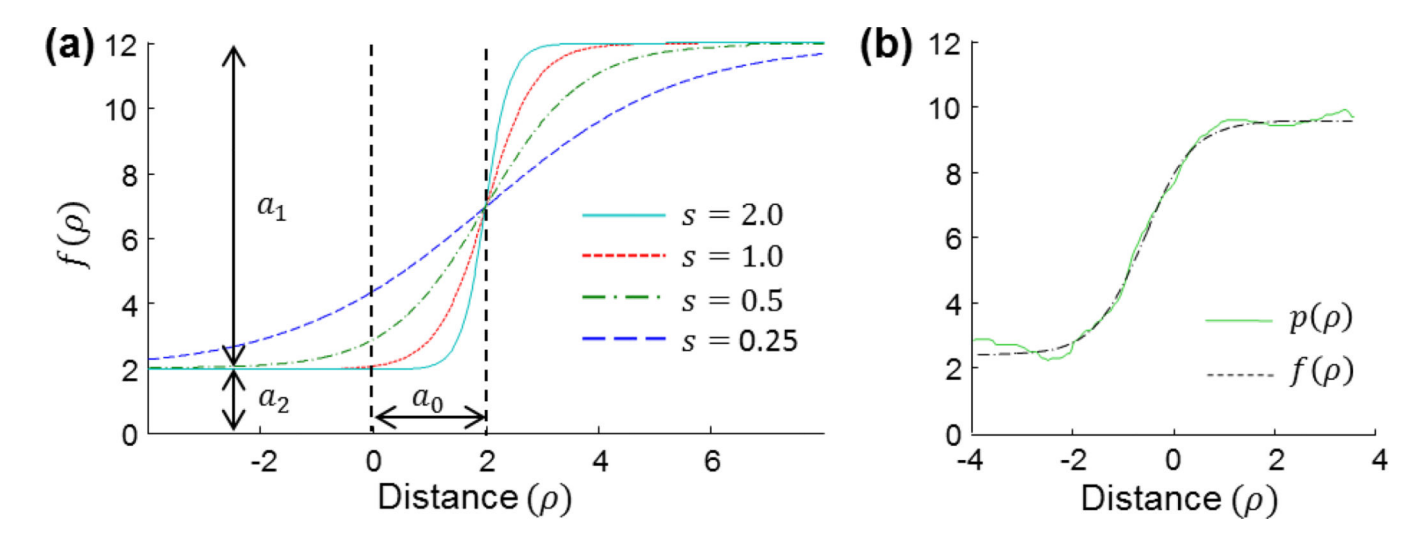


Figure 3. A visual representation of Step-2. (a) A 128 × 128 edge map  $g_f(x, y)$  from Figure 1f, with 28 non-zero edge pixels. One of the possible 28 line segments, drawn locally orthogonal to the edge, is also shown. (b) An intensity profile  $p(\rho)$ , read along the line segment. For this example, the intensity is supposedly read from the hypothetical image on which  $g_f(x, y)$  is based.



**Figure 4.** Parametric modeling of edge profile,  $p(\rho)$ . (a) The sigmoid function described by Equation 5 for four different values of sharpness parameter s. (b) Least-squares fitting of  $p(\rho)$ , from Figure 3, with a sigmoid function,  $f(\rho)$ .

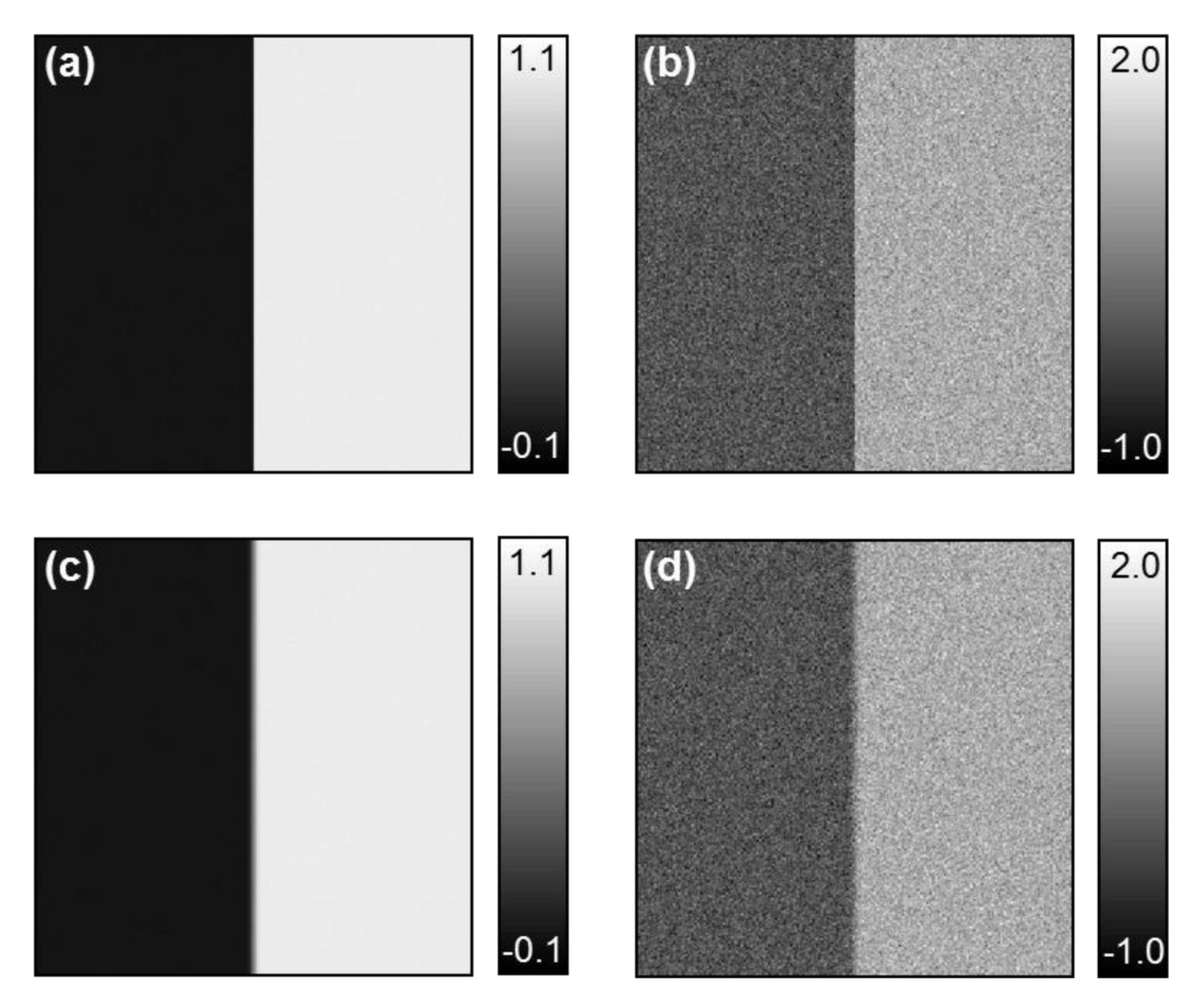
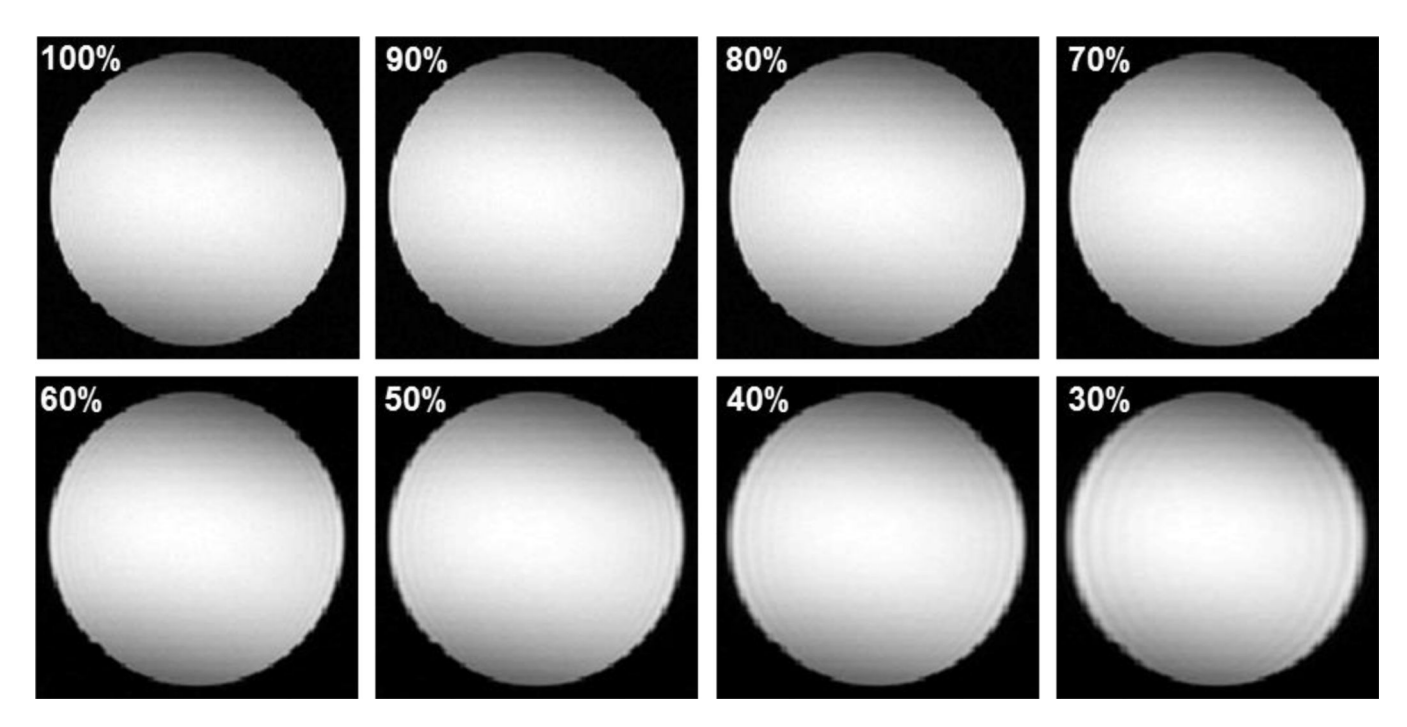


Figure 5. A 256 × 256 phantom with varying levels of edge blurring  $(\sigma_b)$  and additive noise  $(\sigma_n)$ . (a)  $\sigma_b = 0.4$  pixels,  $\sigma_n = 4 \times 10^{-3}$ . (b)  $\sigma_b = 0.4$  pixels,  $\sigma_n = 256 \times 10^{-3}$ . (c)  $\sigma_b = 1.8$  pixels,  $\sigma_n = 4 \times 10^{-3}$ . (d))  $\sigma_b = 1.8$  pixels,  $\sigma_n = 256 \times 10^{-3}$ .



**Figure 6.**A water bottle phantom reconstructed from different numbers of PE steps. The number (top left corner) represents the percentage of PE steps included in the reconstruction. The phase encoding was applied in the horizontal direction.

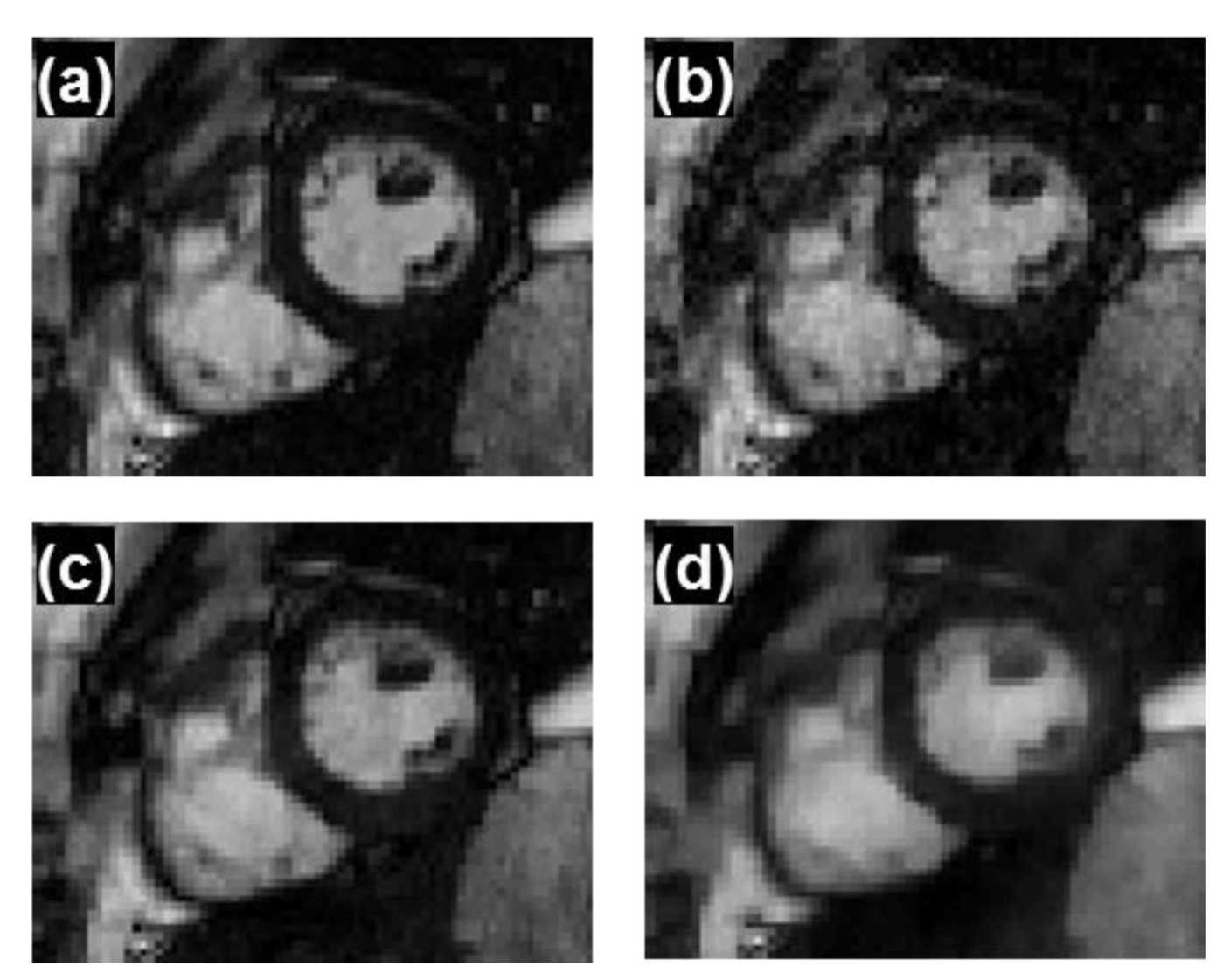
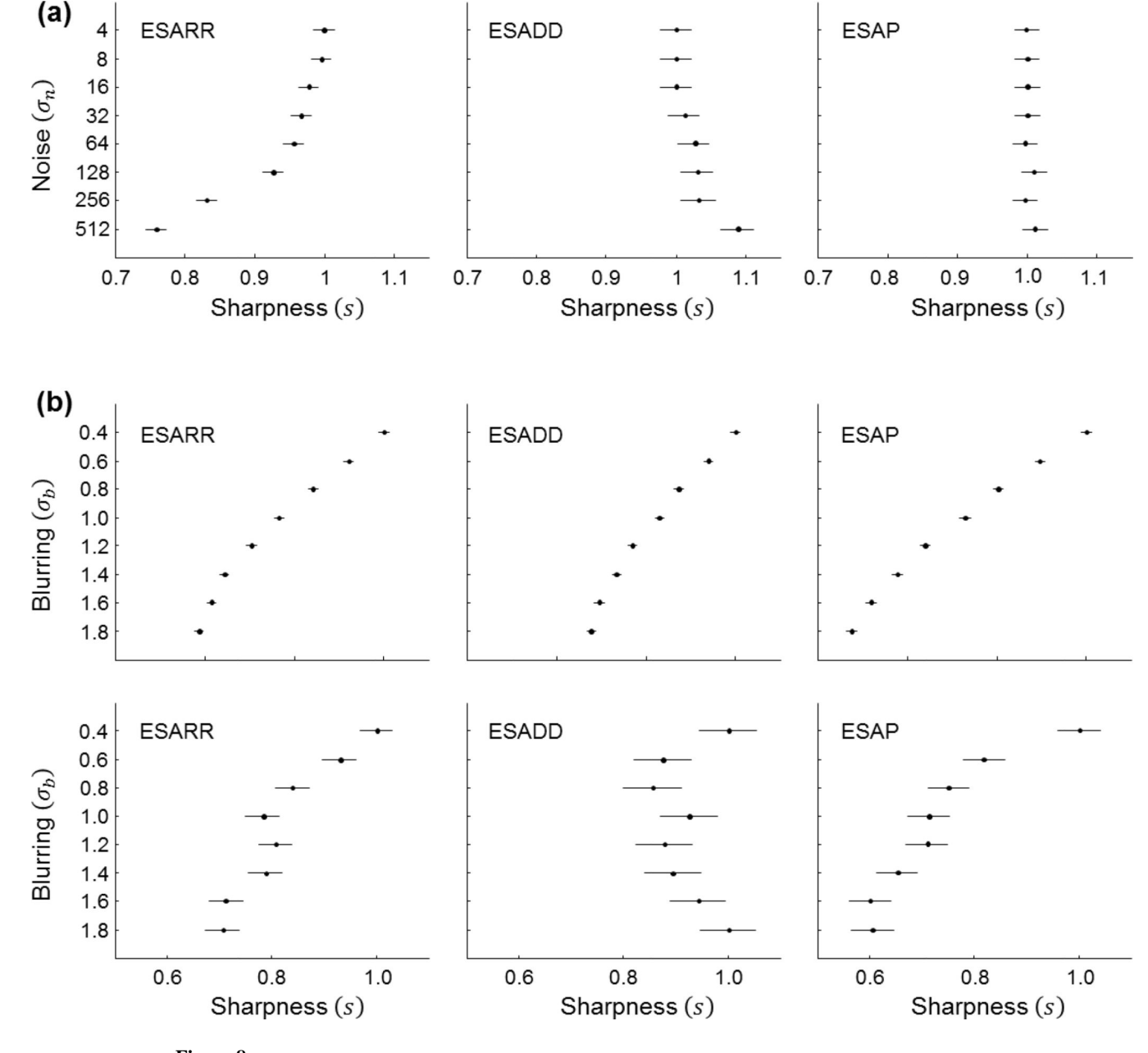


Figure 7. MRI cine reconstruction results with different regularization strengths,  $\lambda$ . (a) A 54 × 74 ROI from one of the fully sampled reference frames. (b) Reconstruction with  $\lambda = 1 \times 10^{-2}$ . (c) Reconstruction with  $\lambda = 10 \times 10^{-2}$ . (d) Reconstruction with  $\lambda = 100 \times 10^{-2}$ .



**Figure 8.** MCT results for three different sharpness methods. (a) Results for  $\sigma_b = 0.4$ , with eight different levels of additive noise. (b) First row: Results for  $\sigma_n = 128 \times 10^{-3}$ , with eight different levels of blurring. All comparison intervals are disjoint except for the last two entries ( $\sigma_b = 1.6$  and  $\sigma_b = 1.8$ ) of ESADD. Second row: Results for  $\sigma_n = 512 \times 10^{-3}$ , with eight different levels of blurring.

40 30

0.2

0.4

0.6

Sharpness (s)

8.0

Page 21 Ahmad et al.

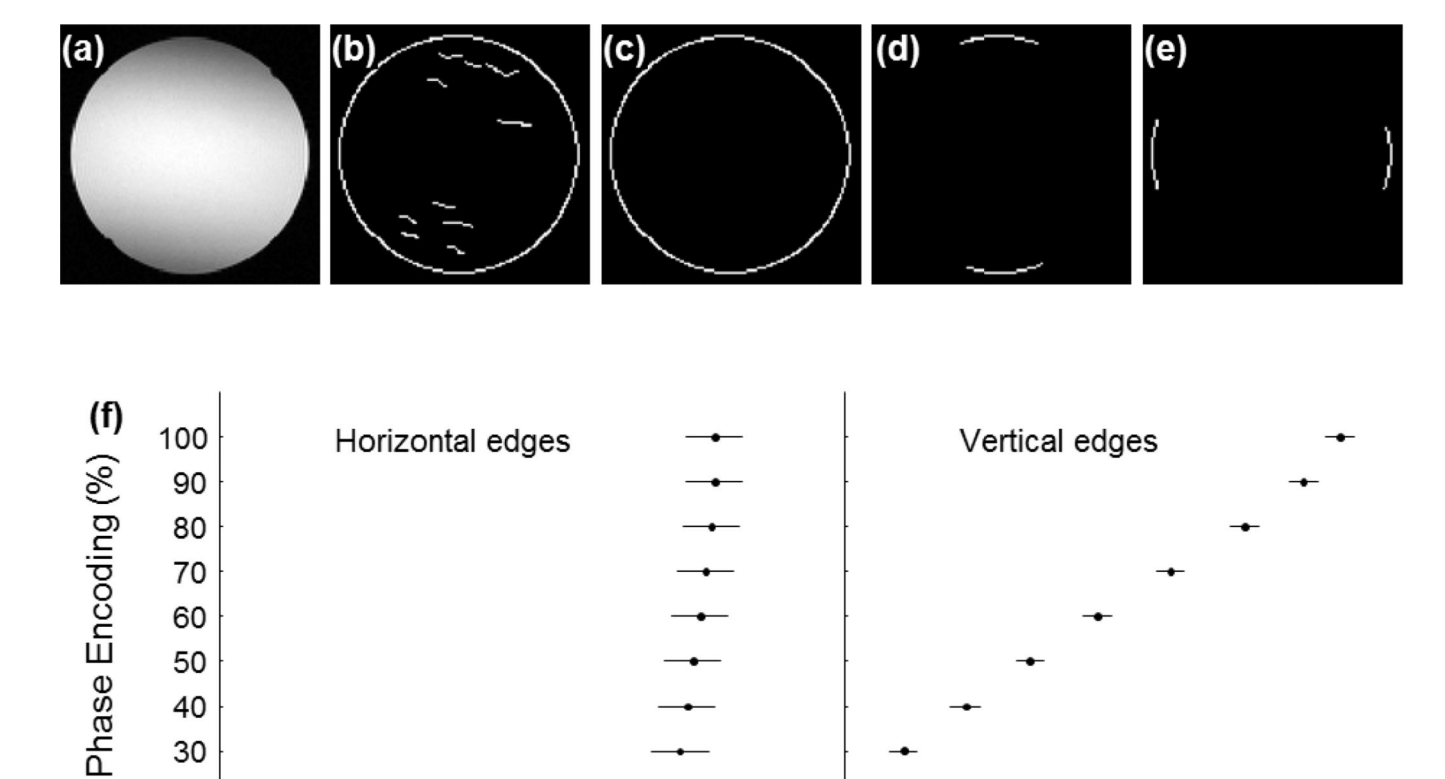


Figure 9. Impact of reduction in the number of PE steps on the sharpness of vertical and horizontal edges. (a) The image reconstructed from 100% PE steps. (b) Edge map, g(x,y), computed from the Figure 9a using CED. (c) User selected EOI. (d) Edges after directional constraints are imposed by setting  $\theta = (75^{\circ}, 105^{\circ}) \cup (255^{\circ}, 285^{\circ})$  to select edge sections with nearhorizontal orientation. (e) Edges after directional constraints are imposed  $\theta = (-15^{\circ}, 15^{\circ})$ ∪ (165°, 195°) to select edge sections with near-vertical orientation. (f) MCT results comparing the sharpness measured by the ESAP method for the horizontal edges (Figure 9d) and vertical edges (Figure 9e).

1

0.2

0.4

0.6

Sharpness (s)

8.0

1

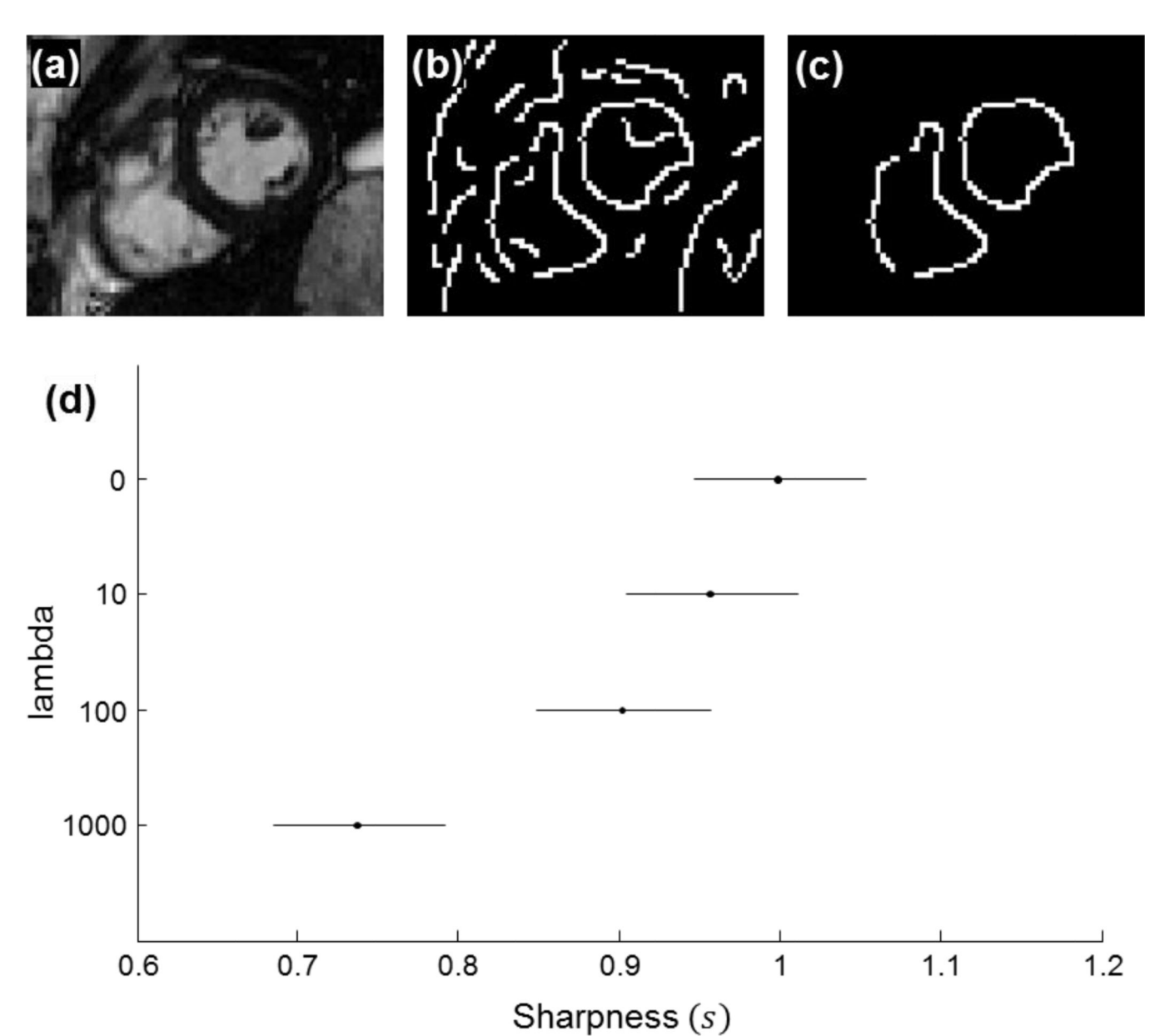


Figure 10. Sharpness measurement for myocardial boundary in MRI cine. (a) CED-based edge map for the first frame shown in Figure 7. (b) User selected myocardial boundary. (c) User selected myocardial boundary with  $\theta = (0^{\circ}, 360^{\circ})$ . (d) Results of MCT test.